Simple analytic model for peristaltic flow and mixing

Ruy Ibanez, Mohammad Shokrian ⓘ, Jong-Hoon Nam, and Douglas H. Kelley ⓘ[*]
Department of Mechanical Engineering, University of Rochester, Rochester, New York 14620, USA

Peristaltic flows occur when fluid in a channel is driven by periodic, traveling wall deformations, as in industrial peristaltic pumps, urethras, stomachs, and cochleae. Peristaltic flows often vary periodically at every point in space but nonetheless cause net transport and mixing of solutes because of Lagrangian (Stokes) drift. Direct numerical simulation can predict peristaltic flows but is computationally expensive, particularly for determining functional relationships between drive parameters and transport or mixing. We present a simple analytic model of peristaltic flow that expresses flow velocity and drift velocity in terms of deformation speed and amplitude. The model extends beyond prior studies by allowing arbitrary wave forms via Fourier series. To validate our analytic model, we present experiments and simulations; both closely match the analytic model over a range of deformation speeds and amplitudes. We demonstrate the applicability of the model by quantifying variations in the thickness of the reflux region (where fluid drifts opposite the direction of travel of deformations) and by modeling mixing in the cochlea, which is promoted by peristaltic flow.

I. INTRODUCTION

The goal of this study is to develop an analytic model with which we can predict peristaltic flows over a range of parameters relevant to small-scale biological systems, without requiring full fluid simulations. A successful model should agree with both experiments and simulations.

Peristaltic flow can occur when a fluid-filled channel is subjected to periodic, traveling deformations at its boundaries. Peristaltic flow occurs in a wide variety of natural and industrial systems, including the urethra [1], the stomach [2], perivascular spaces surrounding arteries in the brain [3,4], the inner ear [5–8], and peristaltic pumps [9,10]. Prior studies have considered peristaltic flows in these and other applications, sometimes developing analytic models. Shapiro *et al.* [9] developed a comprehensive analytic model for peristaltic flows, applicable when boundary deformations travel slowly and have large wavelength. From their idealized model, those authors postulated that peristaltic flows could cause mixing in biological systems. Fung and Yih [11] were likewise motivated by biological applications, focusing on reflux regions where fluid flow opposes the wave propagation direction. Those authors developed a model applicable when boundary deformations travel rapidly, have large wavelength, and have small amplitude. Some of their conclusions differed with those of Shapiro *et al.* Ayukawa *et al.* [12] performed analysis and experiments for the case when deformations travel rapidly, building an analytic model using sources in potential flow. They found reflux near the moving boundary. Takabatake *et al.* [13,14] used numerical methods to study the effects of domain geometry and flow parameters on peristalsis. They found that Reynolds number and geometry affects the behavior of particle transport and that for certain parameters it is possible to produce mixing. Selverov and Stone [15] focused on applications to microfluidic channels using
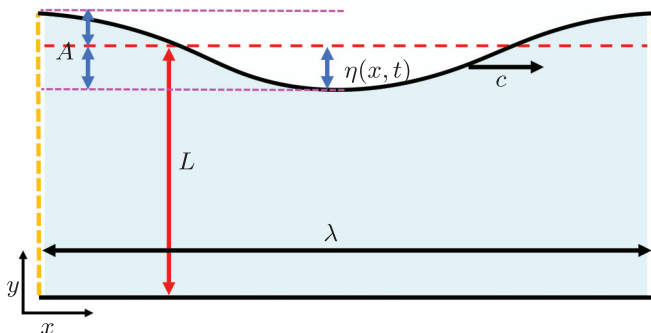
---

*d.h.kelley@rochester.edu

FIG. 1. Sketch of the analytic model's domain. The domain is an infinite two-dimensional channel of mean width L which is periodic in the x direction, with a spatial period λ. Fluid flows because one boundary is deformed in a periodic shape $\eta(x, t)$ moving with constant speed c in the x direction and characteristic amplitude A.

microelectromechanical systems (MEMS). Those authors produced an analytic model applicable when the Reynolds number and wavelength are large and the deformation amplitude is small. Their results show that the peristaltic action can be used for mixing in a channel with finite length. Qing and Damodaran [16,17] demonstrated the effectiveness of using numerical simulations in circular peristaltic channels. Their results show that simple models such as Shapiro's [9] can be extended to non-Newtonian fluids. Another modeling extension is shown in Yasmin *et al.* [18], which implements many physical elements, such as chemical dynamics and magnetohydrodynamics, to an analytic peristalsis model. In our study we use similar numerical techniques and extend the analysis to applications of fluid mixing. Lozano [1] performed analytic and experimental analysis of peristaltic flow in the context of the urethra. He found that particle transport due to peristalsis can play an important role in the distribution of bacteria in the urethra. Edom *et al.* [6] and Sumner *et al.* [8] developed models to study the effect of oscillatory flows in the cochlea, a part of the inner ear. They found that nonlinear streaming can be a mechanism for transport with potential applications to drug delivery.

Expanding on these prior studies, we present a simple analytic model for peristaltic flows that is computationally inexpensive and allows arbitrary deformation shapes, not only sinusoids. The model is precise for the case when deformations travel rapidly, have large wavelength, and have small amplitude. We validate the accuracy of our model using detailed numerical and experimental methods, and demonstrate the relevancy of the model on an example physiological problem. In the following sections we derive the model (Sec. II) and then describe the experimental methods (Sec. III) and numerical methods (Sec. IV) we use to validate it. We discuss validations of the model and its application for estimating mixing characteristics in a biologically motivated problem: flow in the cochlea (Sec. V) and end with a few concluding remarks (Sec. VI)

II. ANALYSIS OF THE PROBLEM

The peristaltic system we consider is modeled as a two-dimensional channel of width L in the y direction and periodic in the x direction, with a spatial period equal to the deformation wavelength λ. Here (x, y) are Cartesian coordinates. The boundary having equilibrium position $y = L$ is deformed in the shape of a wave with shape $\eta(x, t)$. A is the characteristic amplitude of the shape $\eta(x, t)$ traveling at speed c, as shown in Fig. 1; here t is time. We consider the case in which the boundary at $y = 0$ is a rigid wall with a no-slip boundary condition such that $u(x, 0, t) = v(x, 0, t) = 0$, where $u(x, y, t)$ and $v(x, y, t)$ are the velocity components in the x and y directions, respectively. Periodic boundary conditions imply that the velocity of the fluid is the same at each end of the domain: $u(0, y, t) = u(\lambda, y, t)$ and $v(0, y, t) = v(\lambda, y, t)$. We define the Reynolds number as $\text{Re} = cL^2/\nu\lambda$,

where ν is the kinematic viscosity of the fluid. Note that other researchers have considered the symmetric case [9], where both boundaries are deformed. The model we present can be used to solve the symmetric case as well, as described in Appendix C.

The first difficulty in modeling the system shown in Fig. 1 is determining how to treat the moving boundary. To simplify, we perform an expansion of the boundary condition, which defines the shape and motion of the moving boundary:

$$u(x, L + \eta, t) \approx u(x, L, t) + \eta \frac{\partial}{\partial y} u(x, L, t) + \cdots,$$

$$v(x, L + \eta, t) \approx v(x, L, t) + \eta \frac{\partial}{\partial y} v(x, L, t) + \cdots.$$

For both components we retain only the leading term, yielding $u(x, L + \eta, t) \approx u(x, L, t) = 0$ and $v(x, L + \eta, t) \approx v(x, L, t) = \partial \eta / \partial t$. These key approximations in our analytic model allow us to treat the boundary as spatially fixed. We account for the velocity imposed on the fluid by the wall deformation as it changes over time, but we neglect changes to the domain shape and size caused by the wall deformation. That is, we impose a flux condition at the moving boundary. Moreover, these approximations allow us to treat fluid at the boundary as being forced only in the y direction. In other cases, as in large deformations and short wavelengths, significant stretching of the boundary would cause u to be nonzero at the boundary, as demonstrated by Taylor [19]. Therefore the accuracy of the model is limited to cases of small deformation as defined by $\epsilon = A/L \ll 1$, long wavelengths as defined by $L/\lambda \ll 1$, and high Reynolds number Re $\gg 1$.

We solve the system in a reference frame moving at speed c to eliminate time dependence from the equations. This means that the solution must be periodic in x and t such that

$$u(x_1, y, t_1) = u(x_2, y, t_2),$$
$$v(x_1, y, t_1) = v(x_2, y, t_2), \tag{1}$$

where $t_2 = (x_2 - x_1)/c + t_1$. The same assumption has been made in previous studies and shown to be a reasonable approximation [9,11,15].

We simplify the problem by assuming the flow to be inviscid and irrotational, restricting the applicability of our model to cases where the Reynolds number is large (Re $\gg 1$). The subscripts $\{x, y, t, \chi\}$ signify partial derivatives. The coordinate along the channel length, in the frame moving with speed c, is $\chi = x + ct$; other quantities labeled with * are also in the moving frame. In that frame the wall deformation has no time dependence, and we presume that the same is true of all other quantities. In the next section we apply a boundary layer correction, but at this point we express the velocity in terms of a stream function $\psi(x, y, t)$: $u = -\psi_y$ and $v = \psi_x$. The stream function is governed by

$$\psi_{xx} + \psi_{yy} = 0. \tag{2}$$

Equation (2) can be solved in the moving frame using separation of variables, where ψ^* can be represented as the product of two single-variable functions: $\psi^*(\chi, y) = \sum_{n=0}^{\infty} X_n(\chi) Y_n(y)$. Thus the problem can be expressed as $-X_n(\chi)/X_n(\chi)_{xx} = Y_n(y)_{yy}/Y_n(y) = \mu$, where μ is a separation constant. The signs chosen for $X_n(\chi)$ and $Y_n(y)$ are dictated by the fact that the problem must be periodic in χ, in other words, in space (x direction) and time t. The negative sign ensures that the χ part of the solution consists of sines and cosines and the y part of the solution consists of the equivalent hyperbolic sines and cosines.

The function that describes the moving boundary η_t^* is expressed as a Fourier series, such that

$$\eta_t^* = \sum_{n=0}^{\infty} \frac{n\pi}{\lambda} C_n \sin\left(\frac{n\pi}{\lambda}\chi\right) + \sum_{n=0}^{\infty} \frac{n\pi}{\lambda} D_n \cos\left(\frac{n\pi}{\lambda}\chi\right),$$

where n is a non-negative integer. The C_n and D_n terms are obtained by

$$C_n = \frac{1}{\lambda} \int_0^\lambda \sin\left(\frac{n\pi\chi}{\lambda}\right) \eta_t^*(\chi)\, dx, \tag{3}$$

$$D_n = \frac{1}{\lambda} \int_0^\lambda \cos\left(\frac{n\pi\chi}{\lambda}\right) \eta_t^*(\chi)\, dx. \tag{4}$$

We likewise express the separated solutions as Fourier series:

$$X(\chi) = \sum_{n=0}^\infty X_n(\chi) = \sum_{n=0}^\infty \gamma_{n,1} \sin(\mu\chi) + \gamma_{n,2} \cos(\mu\chi),$$

$$Y(y) = \sum_{n=0}^\infty Y_n(y) = \sum_{n=0}^\infty \gamma_{n,3} \sinh(\mu y) + \gamma_{n,4} \cosh(\mu y).$$

The γ factors are constants that are determined using boundary conditions, which are in the moving frame. The boundary conditions of the problem in the moving frame can be described by

$$\psi_x^*(\chi, 0) = 0, \tag{5}$$

$$\psi_x^*(\chi, L) = \eta_t^*(\chi), \tag{6}$$

$$\psi_y^*(\chi, 0) = 0, \tag{7}$$

$$\psi_y^*(\chi, L) = 0, \tag{8}$$

$$\psi^*(0, y) = \psi^*(\lambda, y), \tag{9}$$

$$\psi_x^*(0, y) = \psi_x^*(\lambda, y), \tag{10}$$

$$\psi_y^*(0, y) = \psi_y^*(\lambda, y). \tag{11}$$

The boundary condition given by Eq. (6) requires $\mu = n\pi/\lambda$. Applying the no-penetration boundary condition at $y = 0$ [Eq. (5)] leads to $\gamma_{n,4} = 0$. The problem can be reduced to

$$X_n(\chi) Y_n(y) = C_n \sin(\mu\chi) \sinh(\mu y) + D_n \cos(\mu\chi) \sinh(\mu y).$$

The Fourier series representation allows wall deformations of arbitrary shapes, as long as they are nondispersive (all Fourier components travel with the same speed c). The general solution to the problem in the moving frame is then

$$\psi^*(\chi, y) = -\sum_{n=0}^\infty \frac{C_n}{\mu} \operatorname{csch}(\mu L) \cos(\mu\chi) \sinh(\mu y) - \sum_{n=0}^\infty \frac{D_n}{\mu} \operatorname{csch}(\mu L) \sin(\mu\chi) \sinh(\mu y), \tag{12}$$

which, in the stationary frame, becomes

$$\psi(x, y, t) = -\sum_{n=0}^\infty \frac{C_n}{\mu} \operatorname{csch}(\mu L) \cos[\mu(x - ct)] \sinh(\mu y)$$

$$- \sum_{n=0}^\infty \frac{D_n}{\mu} \operatorname{csch}(\mu L) \sin[\mu(x - ct)] \sinh(\mu y). \tag{13}$$

This solution describes any flow that is inviscid and irrotational, resulting from nondispersive wall deformations of arbitrary shape.

For the simple case of a traveling cosine shape, $C_n = 0$ for all $n \neq 2$ and $D_n = 0$ for all n, so the deformation is $\eta(x, t) = A \cos(\alpha x - \omega t)$ and $\eta_t(x, t) = -A\omega \sin[\alpha(x - ct)]$, where the wave number is $\alpha = 2\pi/\lambda$ and the frequency is $\omega = 2\pi c/\lambda$. The inviscid solution is then

$$\psi^*(\chi, y) = -\frac{A\omega}{\alpha} \text{csch}(\alpha L) \cos(\alpha \chi) \sinh(\alpha y),$$

$$\psi(x, y, t) = -\frac{A\omega}{\alpha} \text{csch}(\alpha L) \cos(\alpha x - \omega t) \sinh(\alpha y). \tag{14}$$

Near boundaries, viscosity and rotation typically play important roles, so the solution given by Eq. (14) is not an accurate model. To improve upon it, we next add a Stokes boundary layer correction by solving the viscous problem locally at $y = 0$ and $y = L$, then we use a superposition of solutions, where we sum the inviscid flow solution calculated using Eq. (2) and the viscous layer solutions. For reference, the boundary layer correction is equivalent to solving Stokes' second problem with the appropriate boundary conditions. For a periodic solution we can solve the viscous problem, where the governing equation is

$$u_t = \nu u_{yy}.$$

We define the superposition of the solutions to be $u_f = u - u_1 - u_2$, where the local solutions near $y = 0$ and $y = L$ are $u_1(x, y, t)$ and $u_2(x, y, t)$, respectively. We apply a no-slip boundary condition at $y = 0$ and $y = L$ such that $u_1(x, 0, t) = u_2(x, L, t) = 0$. We also require that viscous solutions match the inviscid solution: $u_1(x, y, t) = u(x, y, t)$ as $y \to \infty/\delta$, and $u_2(x, y, t) = u(x, y, t)$ as $y \to -\infty/\delta$. For a traveling cosine wave [Eq. (14)], the resulting local solutions are

$$u_1 = A\omega \, \text{csch}(\alpha L) e^{-y/\delta} \sin(\alpha x - \omega t + y/\delta), \tag{15}$$

$$u_2 = A\omega \, \text{csch}(\alpha L) \cosh(\alpha L) \ e^{-(y-L)/\delta} \sin[\alpha x - \omega t + (y - L)/\delta], \tag{16}$$

where

$$\delta = \sqrt{2\nu\omega^{-1}} \tag{17}$$

is the penetration length of the viscous solution. Local solutions for arbitrary traveling waves take similar forms and are straightforward to calculate using the Fourier series approach.

The result is a good approximation as long as the boundary layer remains small compared to the channel width, typically true when $\text{Re} > 10$. In Eq. (15) the exponential factor decays to 0.01 at approximately $y = 4\sqrt{\delta}$. Similarly, in Eq. (16) the exponential factor decays to 0.01 at approximately $y - L = 4\sqrt{\delta}$. Thus the model is applicable with error on the order of 1% as long as $L > 8\sqrt{\delta}$.

This boundary layer correction demands that we modify the velocity field in v to ensure that the flow is divergence-free, because $u_{f,x} + v_y \neq 0$. Thus we replace v with the equivalent viscous corrected velocity v_f, which is obtained by integrating the continuity equation such that $v_f = -\int u_{f,x} \, dy$. The resulting expression is lengthy but straightforward to calculate, as shown in Appendix B. With this continuity correction, the boundary condition at the moving wall [Eq. (6)] is no longer satisfied exactly but is only approximately. The small discrepancy is proportional to the Reynolds number and is negligible as long as $\text{Re} > 10$, as discussed in the Appendix, Sec. B.

Our analytic model is consistent with our expectations for small-amplitude peristalsis in that it does not produce any net flux in the Eulerian sense: the average velocity over one cycle of the temporally periodic forcing is zero at any fixed point in space. That said, our model is also consistent with the general expectation in that it does produce Lagrangian drift, which is expressed as fluid elements experiencing nonzero net displacement through the course of each cycle. Dividing that displacement by the cycle period, we can define a Lagrangian mean velocity [20], which describes how a particle would be displaced over one cycle given an initial position. Though the net displacement of a fluid element during one cycle is always smaller than the length of
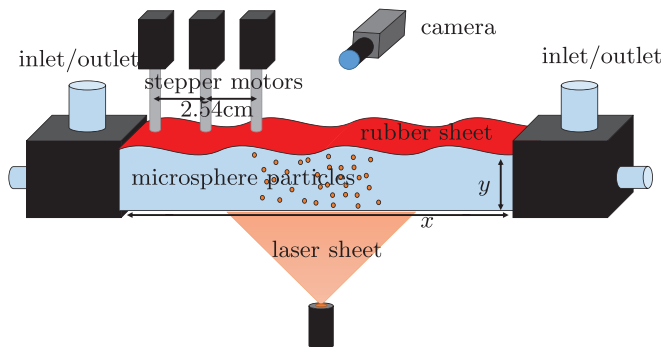
FIG. 2. Sketch of the experimental apparatus. Not shown are the tubing and water reservoirs that allow for the system to be filled and to produce different pressure boundary conditions if desired. Flow is driven via the actuation of the stepper motors, which deform the rubber sheet to produce a shape that closely approximates a periodic wave traveling with constant speed in the x direction.

the path traveled during that cycle, long-term displacements over many cycles can be accurately quantified using the Lagrangian mean velocity. To do so, we use the Lagrangian mean velocity to map the locations of fluid elements at the beginning of a cycle to the locations of those same elements at the end of a cycle. Applying the map repeatedly, via integration of tracer particle motion in the analytically obtained velocity field with a fourth-order Runge-Kutta scheme, we can accurately estimate the Lagrangian mean flow over many cycles. Doing so significantly reduces the computational cost of calculating displacements over multiple periods from simulation results and avoids the need for lengthy experimental measurements. Because the Lagrangian mean velocity is steady, its streamlines also approximate path lines.

III. EXPERIMENTAL METHODS

We validate our analytic model using laboratory experiments driving peristaltic flow. Our experimental apparatus, shown in Fig. 2, consists of a transparent square channel with dimensions 94.6 cm × 2.54 cm × 2.54 cm. The top wall is made of a flexible rubber (thickness 1.6 mm, durometer 40A, from McMaster-Carr) and is actuated by 14 translation stages driven by stepper motors. The stepper motors can induce a discrete form of a traveling wave deformation. The channel is filled with deionized water and microspheres from the manufacturer Cospheric. The particles are of diameter $d = 115.5 \pm 9.5 \, \mu$m for flow visualization. The maximum Stokes number in our experiments of the particles is St $= U_s(\rho_p - \rho)d/18\nu\rho < 0.01$, where $\rho_p = 1 \pm 0.01$ g/cc is the particle density, $\rho = 1$ g/cc is the fluid density, and $U_s = 100$ mm/s is a characteristic flow speed. Since St $\ll 1$, we expect the particles to track fluid motion accurately. A laser sheet is projected from below to illuminate the x-y plane at the middle section of the experiment. To capture the motion of the particles we use an Emergent 4000M camera. From videos of particle motion, we produce Eulerian velocity fields via particle image velocimetry (PIV) using the MATLAB version of the open-source code PIVLAB [21]. We also produce Lagrangian particle tracks via particle tracking velocimetry (PTV) using a MATLAB-based predictive tracking algorithm [22]. The channel is filled using reservoirs connected at each end of the apparatus via flexible tubing. The connections and reservoirs allow us to impose different pressure boundary conditions, but in the case of this study we explore only the case in which the pressure is equal at both ends.

We approximate the continuous wall deformation η by actuating the rubber wall at a discrete set of locations (one for each stepper motor), spaced evenly with 2.54 cm separation. Thus, according to the Nyquist criterion, our apparatus can produce deformations η that are superpositions of wavelengths as short as 5.08 cm. To produce wall motion, we use a custom MATLAB code which

determines the necessary steps each motor must take to simulate a continuously deforming wave. The amplitude and wave speed are bound by the stepper motors' ability to produce enough torque to displace the rubber. We use Igus Ds6.35 × 25.4 high helix lead screws to be able to reach high deformation speeds with low friction for smooth displacement.

Our measurements are restricted to the bulk region of the flow, as sections near boundary regions ($y \approx 0$ and $y \approx L$) are experimentally difficult to measure due to visual limitations that preclude accurate particle tracking. We found that ambient temperature gradients in the laboratory drive a slow flow, with velocities up to 0.1 mm/s. We report results only from experiments where the driven flow is much faster than the average particle velocity, in other words, the driven flow is an order of magnitude larger than the background flow. In much of our analysis we phase-averaged PIV velocity data over many cycles (between 25 and 125 cycles) to increase the signal-to-noise ratio. After phase averaging, the dimensionless noise is calculated by averaging in space the standard deviation in time of the non-phase-averaged velocity field. The phase-averaged velocity field $u_{\bar{\theta}}(x, y, t)$ is calculated by taking the average of velocity measurements in the same spatial location, at different points in time with equal phase. Thus $u_{\bar{\theta}}(x, y, t) = \overline{u(x, y, t + j2\pi/\omega)}$ where j is an integer. From the same calculation one can obtain the standard deviation, which can be normalized with respect to the phase-averaged value at each point in space, such that $\text{std}(u_{\bar{\theta}})_{\text{norm}} = \text{std}[u_{\bar{\theta}}(x, y, t), t]/u_{\bar{\theta}}(x, y, t)$. Finally, we calculate the absolute mean standard deviation by averaging over space, thus obtaining single number, in other words $\overline{\text{std}(u_{\bar{\theta}})_{\text{norm}}}$. This gives us an estimate for the noise in our PIV measurements. The resulting deviation ranges from 1% to 5%. The average deviation was calculated using 15 experimentally measured PIV fields, each containing 2706 spatial points and 25 to 125 cycles of data, which averaged approximately 2000 steps in time.

IV. NUMERICAL METHODS

A second validation of our analytic model comes from direct numerical simulations of peristaltic flow. The finite element approach was employed to numerically solve the Navier-Stokes equations:

$$U_t + UU_x + VU_y = \rho^{-1}P_x + \nu(U_{xx} + U_{yy}), \quad V_t + UV_x + VV_y = \rho^{-1}P_y + \nu(V_{xx} + V_{yy}),$$

where P is pressure, U is the velocity component of the fluid in the x direction, V is the velocity component of the fluid in the y direction, and the continuity equation

$$U_x + V_y = 0.$$

A two-dimensional geometry was constructed. L and λ were set to 2.54 and 30 cm, respectively. The length of the channel was chosen to be twice the wavelength to allow for the boundary effects to resolve. All results described below come from the region $\lambda/2 \leqslant x \leqslant 3\lambda/2$, far from the end boundaries. One edge of the rectangular fluid domain was taken as a fixed, no-slip wall. The ends were taken to be open, with zero normal stress. The remaining boundary was taken as a no-slip wall deforming over time according to $A\sin(\alpha x - \omega t)$, where A is the amplitude of the wave. A set of different amplitudes and frequencies was simulated for comparison. The governing equations were solved using COMSOL MULTIPHYSICS on a single computer (Intel Xeon W-2145 processor). The mesh included about 110 000 triangular elements as well as 7000 quadrilateral elements at the location of the boundaries. All the elements were of second order. The typical element size was chosen to resolve the boundary layer thickness for the Stokes second problem δ. The mesh resolution was able to fully capture the velocity gradient at the boundary layers. To ensure convergence to the periodic state, five consecutive cycles were run for each simulation. The time step was chosen as 1/50 of the cycle period after running a series of time-step sensitivity tests. The generalized-α [23] method used for temporal differentiation in this study is a second-order implicit method. Each simulation takes about an hour of computational time for this study.
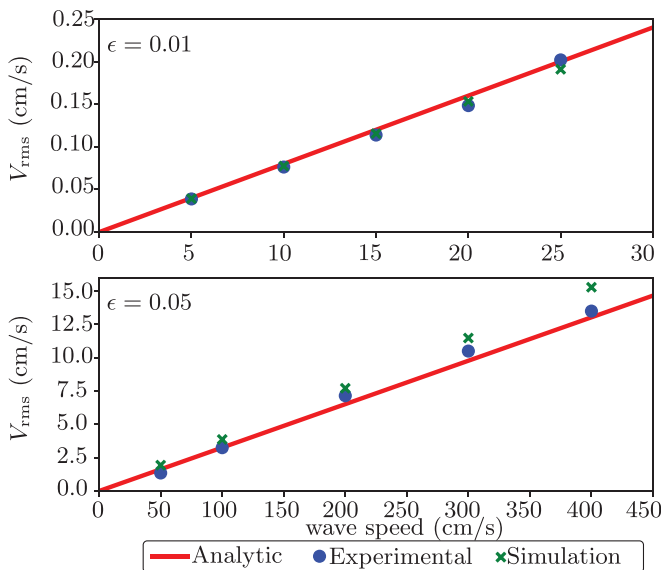
FIG. 3. Comparison of the root-mean-square velocity in the bulk flow region in experiments, modeling, and simulations, with $\epsilon = 0.01$ (top panel) and $\epsilon = 0.05$ (bottom panel). The wavelength was held constant at $\lambda = 30$ cm.

V. RESULTS

A. Eulerian results

We can produce two types of measurements from the experimental data—Eulerian velocity fields and Lagrangian particle paths. First we will consider Eulerian data. We compare the model to experimental measurements only in the region $0.05L \leqslant y \leqslant 0.9L$, due to limitations of optical access, as discussed in Sec. III. We characterize the overall flow speed using the root-mean-square speed $V_{\rm rms} = \overline{(u^2 + v^2)}^{1/2}$, where an overline signifies the spatiotemporal average over the region $0.05L \leqslant y \leqslant 0.9L$. $V_{\rm rms}$ allows us to compare different velocity fields with a single number, as shown in Fig. 3. We find good agreement among the analytic model, experiments, and simulations for the relevant parameter range for the analytic model. To determine the accuracy of the model, we calculate the average normalized difference of measured $V_{\rm rms}$. $V_{\rm rms,exp}$ is the experimentally measured, $V_{\rm rms,sim}$ is the simulation produced, and $V_{\rm rms,anl}$ is the analytically derived $V_{\rm rms}$. The normalized difference between the analytic model and the experimental measurements is given by $\overline{V_{\rm rms,anl} - V_{\rm rms,exp}}/V_{\rm rms,anl} = 5.2\%$. The normalized difference of the simulation to analytic model is given by $\overline{V_{\rm rms,anl} - V_{\rm rms,sim}}/V_{\rm rms,anl} = 5.6\%$, where $\bar{\cdot}$ is the operator for the averaging; in this case the average is taken over all samples. In simple terms, this provides a measurement of error across all of our comparisons between models. We find that the periodicity in time is also present in experimental measurements, as well as the time dependency behaving as a linear spatial shift. We can check if the periodicity relation from Eq. (1) is satisfied by comparing experimentally measured velocities at different times in the same position. When we compare experimental data we find that the average normalized error for measured flows is 2%. We calculate the error by checking the accuracy of the periodicity relation Eq. (1). We sample two experimental data points in the x direction, where each has 61 data points in y at 500 points in time, for 15 different flow parameters. The error is then calculated as $|u(x_1, y, t_1) - u(x_2, y, (x_2 - x_1)/c + t_1)|/\overline{u(x_1, y, t_1), u(x_2, y, t_2)}$, where $\bar{\cdot}$ is the average of the two sampled velocities. The flows we measured in experiments were nearly periodic, with cycle period matching that of the traveling wave on the moving boundary, even for large Reynolds
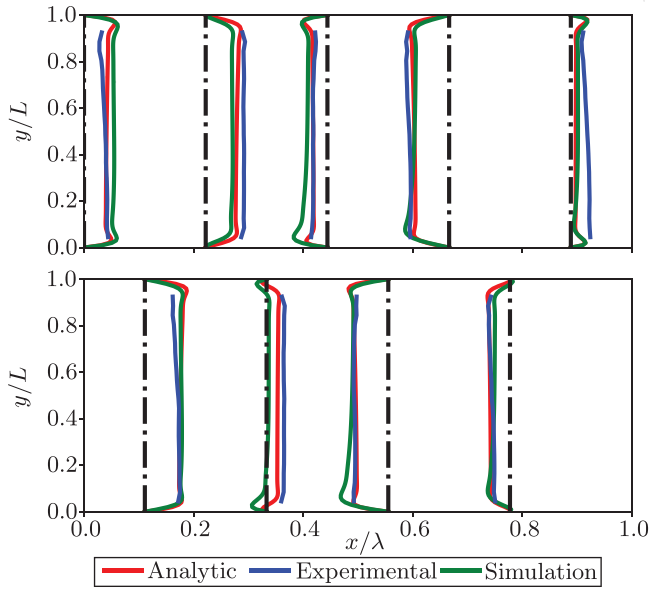
FIG. 4. Comparison of x-direction velocity profiles in experiments, modeling, and simulations. Each black line indicates the location of the corresponding profiles. Profiles are plotted on two separate panels only to allow enlargement for the sake of visibility. Parameters: $c = 20$ cm/s, $\lambda = 30$ cm, $\epsilon = 0.01$.

numbers (Re $\approx 10^4$). To show more detail, we can compare x-direction velocity profiles, as shown in Fig. 4.

Figure 5 shows a comparison of normalized vorticity fields produced by the analytic model and simulation. The normalized vorticity $\hat{w}$ is defined as the vorticity divided by the absolute maximum
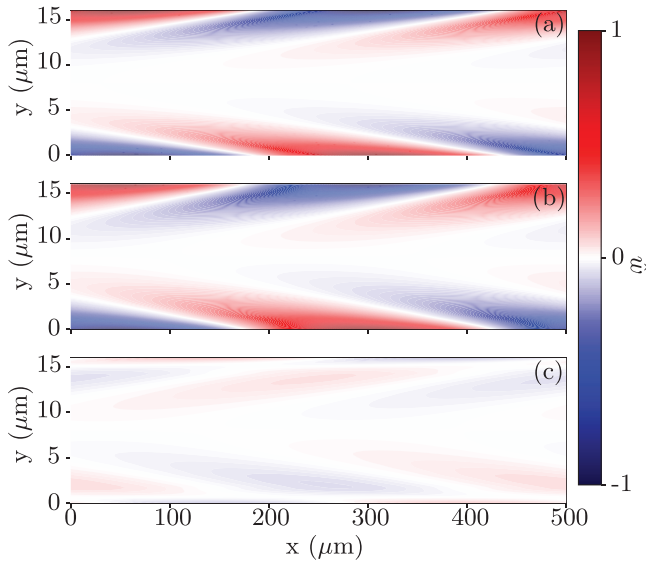

FIG. 5. Comparison of vorticity fields from the analytic model (a) and simulation (b), with the difference plotted in (c). In all three, vorticity is normalized by the absolute maximum vorticity of the model, and $\lambda = 500\,\mu$m, $L = 16\,\mu$m, $\epsilon = 0.13\%$, and $c = 60$ m/s.
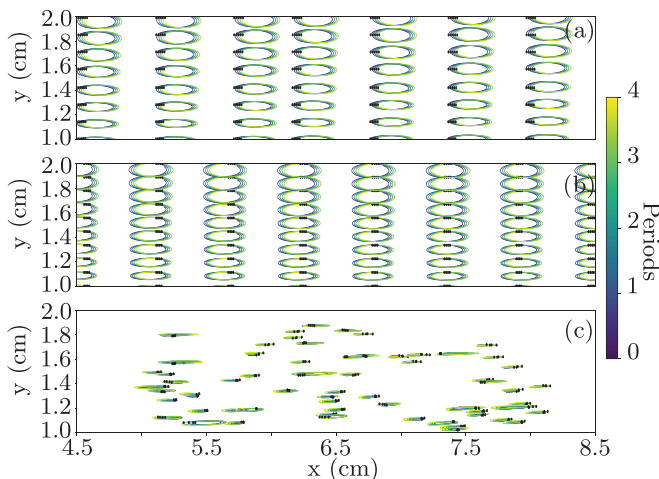
FIG. 6. Examples of (a) simulated, (b) analytic, and (c) experimentally measured particle path lines, with $c = 1$ m/s, $\lambda = 30$ cm, and $\epsilon = 3\%$. Black points mark particle locations a period apart.

vorticity of the analytic model. The results show good agreement, with small differences around the boundary layer likely due to the model approximation limitations.

B. Lagrangian results

To illustrate how to use our model to study mixing, we verify that the analytic model accurately predicts transport by comparing Lagrangian mean flows produced by the analytic model, experimental measurements, and simulation data. We compare the Lagrangian mean flows to previous studies.

Figure 6 shows a few experimentally measured particle paths from the current study. At the end of each cycle, each particle returns to a location close to—but not identical to—its location at the beginning of the cycle. In the region shown, which lies near the center of the domain, the net displacements of most particles are primarily in the direction of increasing x, consistent with the fact that wall deformations travel in the direction of increasing x. These characteristics are consistent with prior studies [9,11].

One characteristic of peristaltic flows is that the Lagrangian mean flow can exhibit reflux, meaning that the particles near the moving boundary drift in the opposite direction as the traveling wave, while the ones in the bulk region move in the same direction as the wave. To explore reflux, we averaged the numerically integrated Lagrangian mean flow over one spatial period in the x direction, yielding the drift velocity profile $u_{\text{drift}}(y)$. Figure 7(a) shows $u_{\text{drift}}(y)$ (normalized by its maximum value, for easier visualization), as produced by our model, over a range of Reynolds numbers. In all cases the model predicts a reflux region. As the Reynolds number increases, profiles of $u_{\text{drift}}(y)$ become flatter in the bulk, where inertial forces come to dominate viscous forces. Meanwhile, boundary layers grow thinner, and velocity variations within boundary layers become steeper. Accordingly, the reflux region shrinks as the Reynolds number increases, as predicted by Shapiro *et al.* [9]. We can quantify that trend by locating the edge of the reflux region, which occurs at $y = y_{\text{edge}}$, with $u_{\text{drift}}(y_{\text{edge}}) = 0$. Figure 7(b) shows the edge location and demonstrates that as the Reynolds number increases, the edge approaches the moving boundary, as expected.

While we performed our analysis using direct integration of the analytic model Eulerian fields, it is possible to analytically calculate the Lagrangian mean field. Applying the Lagrangian mean method described by Andrews and McIntyre [20] and employed by Lighthill [24] to obtain similar results, one can obtain analytic expressions for Lagrangian fields if corresponding Eulerian fields
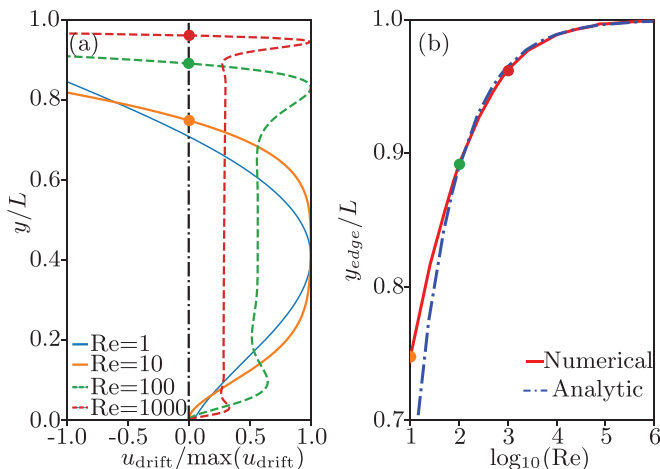
FIG. 7. (a) Comparison of the normalized drift velocity profile $u_{\text{drift}}/\max(u_{\text{drift}})$ at different Reynolds numbers Re. The black line marks the zero velocity point. (b) Location of the edge of the reflux region, as predicted by the analytic model. The red line is obtained through numerical integration of the Eulerian velocity field (u_{drift}). The blue line is the analytic approximation (U_{Lag}). The dots are the edge location for the curves on (a), and the color matches the relevant Reynolds number. As the Reynolds number increases, the reflux region shrinks.

are known. To calculate the Lagrangian mean field one must use the equation

$$U_{\text{Lag}} \approx \overline{\int u(x, y, t)\partial t \frac{\partial u(x, y, t)}{\partial x} + \int v(x, y, t)\partial t \frac{\partial u(x, y, t)}{\partial x}}, \tag{18}$$

where U_{Lag} is the Lagrangian mean field and the overbar is the time average over a period $\omega/2\pi$. In the case of a simple traveling sine wave [$\eta = A\sin(\alpha x - \omega t)$], applying Eq. (18) gives an expression for the Lagrangian mean field. The resulting expression is presented in Appendix C. By inspection one can note that $U_{\text{Lag}} \propto \epsilon^2 c$. Additionally, the derivation shows that one ought to expect a region of reverse drift near the moving boundary. The edge of the reflux region can be analytically estimated to be located at $y_{\text{edge}}/L = 1 - 2\delta/L$, which can also be written as $y_{\text{edge}}/L = 1 - 2/\sqrt{\pi \text{Re}L^2}$, according to Eq. (17). This means that in the region where $y/L > 1 - 2/\sqrt{\pi \text{Re}L}$, the drift direction is expected to be opposite to the wave direction, as shown in Fig. 7. The edge location predicted by the Lagrangian mean method closely matches the edge location calculated via numerical integration of the Lagrangian mean velocity.

We also calculated the Lagrangian mean velocities without the viscous boundary layer correction, finding no reflux; all particles drift in the direction of wave propagation. This suggests that reflux is a consequence of viscosity, consistent with the predictions of Shapiro *et al.* [9]. They also found that for their Re < 1 model, the magnitude of drift was proportional to $\epsilon^2 c$. To explore the variation of drift with c in our models, we averaged the Lagrangian mean flow over the domain $0 \leqslant x \leqslant \lambda$, $0.05L \leqslant y \leqslant 0.9L$ (excluding regions where optical limitations prevent experimental validation). We then calculate the mean Lagrangian drift (averaged over space) in the x direction U_{drift} from the analytic (via numerical integration), experiment, and simulation results, again varying c. The results are shown in Fig. 8. Our model does predict $U_{\text{drift}} \propto c$, and that prediction is borne out by both experiments and simulations, even when the Reynolds number far exceeds the Re < 1 regime considered by Shapiro *et al.* [9].

As predicted by our model and confirmed by experiments and simulations, the net Lagrangian transport is much slower than typical instantaneous Eulerian flow speeds. For example, Fig. 8 shows that for the $\epsilon = 0.05$ case, with $c = 0.05$ m/s, $U_{\text{drift}} = 0.13$ cm/s. But Fig. 3 shows that for the
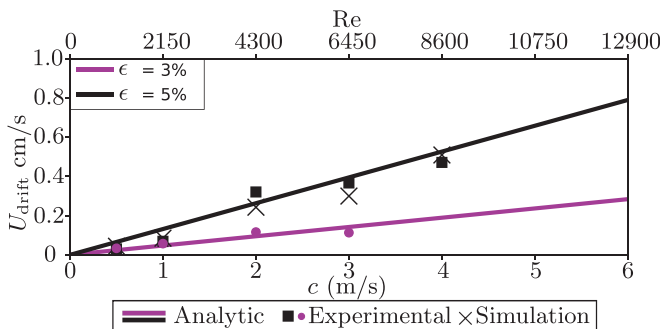
FIG. 8. Variation of the mean drift velocity U_{drift} with wave speed c and normalized deformation amplitude ϵ, and the calculated Reynolds number. The wavelength was held constant at $\lambda = 30$ cm.

$\epsilon = 0.05$ case, with $c = 0.05$ m/s, $V_{\text{rms}} = 1.6$ cm/s. That is, with comparable parameters, U_{drift} is smaller by more than an order of magnitude. The relationship between U_{drift} and V_{rms} is similar for other cases. Prior studies have similarly found that Lagrangian drift is much slower than instantaneous flow speeds [9]. Thus we conclude that peristaltic flows with parameters in the range we consider cause only slow mixing by advection alone. We would expect faster advective mixing when the wave speed is higher, since $U_{\text{drift}} \propto c$. We would expect significantly faster advective mixing when the deformation amplitude is greater, since $U_{\text{drift}} \propto \epsilon^2$. Accordingly, a more recent study found that large-deformation peristalsis of the sort that occurs in the stomach produces fast mixing [2]. Another mechanism for mixing is the combination of advection and diffusion. Below we will use our analytic model to make predictions about mixing by advection and diffusion together, in the same parameter range considered above, with application to one example problem: mixing in the cochlea.

C. Example application: Mixing in the cochlea

As an example of the applicability of our analytic model, we consider mixing in the cochlea, a spiral-shaped structure in the inner ear. At its core is the tunnel of Corti, a fluid-filled channel 6 mm long but just 50 μm across [7]. Note that we will neglect any curvature that is found in the tunnel of Corti. For reference, Manoussaki *et al.* [25,26] studied the impact of curvature on the system, where the strongest effects are found at the extreme edge in the tunnel of Corti and lower frequencies. The cochlea fluid space is a noncircular cavity in bony shells and is partitioned by an elastic structure known as the basilar membrane, which moves much more than any other boundary of the fluid space. Because of its geometric characteristics, the cochlear fluid space has been modeled as a two-dimensional or three-dimensional box with one moving wall [27–30]. Whereas many other physiological fluid channels are subjected to large strain (>0.1), the elastic structures of the cochlea are subjected to small strain (<0.01), compatible with our modeling. Additionally, other channels transport fluids unidirectionally, but net advection in the cochlea is considered minimal (e.g., 1.6 nL/min) [31]. That said, a few studies [6–8,31,32] have explored the physics of steady streaming of the cochlear fluids. As Shokrian *et al.* [7] pointed out in their study of the Corti fluid space, the pronounced wavelength-to-height ratio in this microfluidic space causes the substantial longitudinal fluid velocity. Our attempt to study mixing in the tunnel of Corti was motivated by this longitudinal velocity.

Our example is thus a reasonable approximation for large sections in the cochlea, but one must be mindful of the limitations of ignoring curvature when considering the extreme cases of the system. The channel is lined with inner hair cells, which convert fluid vibrations to neural impulses, relying on the electrochemical gradient between different fluid spaces as their driving force. Maintaining fluid homeostasis by an appropriate mass transport (fluid mixing) can contribute to healthy hearing
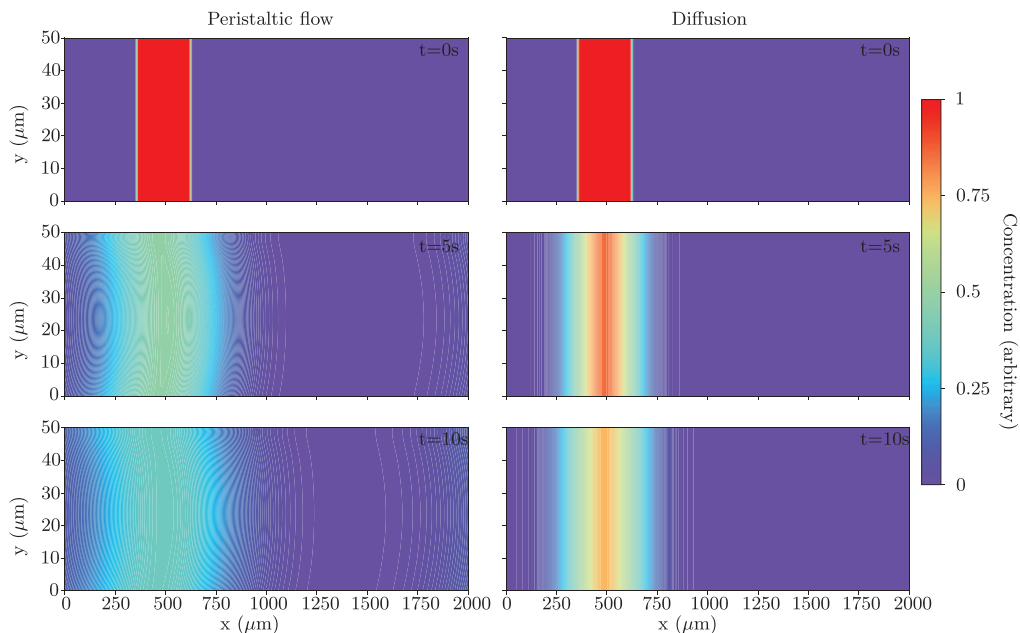
FIG. 9. Change of the concentration of a passive scalar subjected to both diffusion and the modeled Lagrangian mean flow or subjected to diffusion alone. In the case with flow, $\lambda = 200\,\mu\text{m}$, $L = 50\,\mu\text{m}$, $\epsilon = 0.2\,\%$, and $c = 50$ m/s. In both cases, $D = 7 \times 10^{-10}$ m^2/s. Peristaltic flow causes more mixing than diffusion alone.

[7]. The channel is also lined with outer hair cells, which are known to deform the channel walls, producing longitudinal fluid motion along the tunnel of Corti [33]. Some researchers considered that such fluid motion due to cell motility is relevant to cochlear amplification of faint sounds [5]. Others suggested that the vibrations induced by cell motility could drive peristaltic flow, resulting in fluid mixing, which helps cochlear fluid homeostasis [7]. Here we will use our model to estimate the peristaltic flow in the cochlea, then perform advection-diffusion simulations to determine the resulting mixing.

We take relevant parameter values for the cochlea from a prior publication [7]. The width of the tunnel of Corti is $L = 25$–$100\,\mu$m. Deformations of its walls have wavelengths ranging from $\lambda = 0.2$ to 4 cm, a normalized amplitude $\epsilon = 0.2\,\%$, and travel at speeds ranging from $c = 1$ to 100 m/s. Relevant ions in solution have a diffusivity of $D = 7 \times 10^{-10}$ m^2/s. For the example flow we present, the Reynolds number is Re $= 95.6$, $V_{\text{rms}} = 31.1$ mm/s, and $U_{\text{drift}} = 0.027$ mm/s, where the other parameters lie within the range of the cochlea.

To explore mixing in the cochlea, we simulated the spatiotemporal development of ion concentration with an advection-diffusion code. That code uses a first-order forward Euler scheme in time and a second-order finite difference scheme in space; further details are given in Troyetsky *et al.* [34]. The code solves the advection-diffusion equation,

$$\frac{\partial C}{\partial t} = D\nabla^2 C - \mathbf{U} \cdot \nabla C,$$

where C is the concentration field, D is the diffusivity, and $\mathbf{U} = (U, V)$ is the velocity field. Since both diffusion and advection affect the ion concentration, both the diffusivity and the underlying velocity must be provided. We used our analytic model to produce the velocity. More precisely, with the parameters listed above, we used the model to produce a flow field varying over space and

time. From it we calculated the Lagrangian mean flow, which we used in the advection-diffusion simulation.

The results are shown in Fig. 9. We find that the peristaltic action enhances mixing, compared to diffusion alone. Enhanced mixing is likely due to Taylor dispersion [35,36], a mechanism in which shear in one direction (here, the x direction) creates concentration gradients in another direction (here, the y direction) which are rapidly smoothed by diffusion, resulting in faster mixing. Our finding of enhanced mixing is consistent with prior studies [6,7].

We can estimate the development of ion concentration over time using the Lagrangian mean flow calculated from the velocity field produced by our analytic model. Using the Eulerian velocity field would capture more of the flow details and produce more accurate results. However, doing so would also require much more computational time, since accuracy would require many time steps for each cycle. The Lagrangian mean flow does not capture the full paths of ions but only their net displacement by advection over each cycle. Thus it produces accurate results as long as ion displacements caused by diffusion during a cycle are much smaller than displacements caused by advection. To quantify the accuracy of this approximation, we calculated L_{drift}, which is the average length traveled by a fluid element during one cycle. We also calculated the characteristic length of diffusion over one cycle, $L_{\mathrm{diffusion}} = \sqrt{D\lambda/c}$. We find that for high-Reynolds-number flows (high frequency), $L_{\mathrm{drift}} > L_{\mathrm{diffusion}}$, implying that the approximation is reasonable. For our example scenario, we find $L_{\mathrm{drift}} = 1$ μm to be an order of magnitude larger than $L_{\mathrm{diffusion}} = 0.1$ μm. The methodology we use is orders of magnitude less expensive computationally than the alternative. Calculating the Lagrangian mean flow from the velocity field produced by our analytic model takes about two minutes, far less time than a corresponding simulation using the finite element approach would take. For example, the finite element computations required for Fig. 8 took about five hours.

VI. CONCLUSION

We have presented a simple model for peristaltic flows in an open channel. We demonstrated that the model can be combined with simple computational techniques to provide fast and accurate estimates of mixing in peristaltic systems. We validated the model by comparing to both simulations and experiments. We demonstrated the model's applicability by using it to study mixing in the cochlea, finding faster mixing with peristaltic flow than with diffusion alone, consistent with previous studies [7]. We also provided measurements on Lagrangian transport and the behavior of reflux. Understanding the characteristics of reflux could be critical to optimizing mixing, as spatiotemporal distributions of the flow can be important, as discussed in Arrieta *et al.* [2].

Our model can help to better understand and develop future hypotheses about the role of peristalsis in biological and mechanical systems. Preliminary analysis shows that the Lagrangian characteristics of complicated wave shapes can play an important role in mixing efficiency. It is possible that some shapes may lead to better mixing than others. In the future, we plan to use the methods demonstrated in this paper to estimate optimal parameters for mixing in microfluidic peristalsis.

The data that support the findings of this study are available from the corresponding author upon reasonable request.

ACKNOWLEDGMENTS

APPENDICES

Here we present expressions to the solution that were too spacious to be included in the main text.

APPENDIX A: EXTENDED EXPRESSIONS OF THE ANALYTIC MODEL

For $\eta_t(x, t) = A\omega \sin(\alpha x - \omega t)$, the full corrected y velocity is $v_f(x, y, t) = -\int u_x(x, y, t) dy$, which is obtained using the continuity equation. The expanded expression is below in Eq. (A1). ξ is the integration constant, which is solved for by applying the no-penetration condition $v_f(x, 0, t) = 0$. Note that the y velocity of the viscous solution does not exactly match the original boundary condition such that

$$
v_f(x, y, t) = A\omega \operatorname{csch}(\alpha L) \sinh(\alpha y) \cos(\alpha x - t\omega)
$$

$$
+ \frac{\alpha A\omega}{\sqrt{2}\delta} \left[\coth(\alpha L) e^{\frac{L-y}{\delta}} \sin\left(\frac{\pi}{4} - \frac{L-y}{\delta} + t\omega - \alpha x\right) \right.
$$

$$
\left. - \operatorname{csch}(\alpha L) e^{-y/\delta} \sin\left(\frac{\pi}{4} + t\omega - \alpha x - y/\delta\right) \right] + \xi,
$$

$$
\xi = \frac{\alpha A\omega}{\sqrt{2}\delta} \coth(\alpha L) e^{-L/\delta} \sin\left(\frac{\pi}{4} - L/\delta + t\omega - \alpha x\right) - \frac{\alpha A\omega}{\sqrt{2}\delta} \operatorname{csch}(\alpha L) \sin\left(\frac{\pi}{4} - \alpha x + t\omega\right).
$$

$$(\text{A1})$$

The deviation from the original boundary condition is important, since that is the only input into the system. The difference in the viscous boundary condition is calculated by $v(x, L, t) - v_f(x, L, t)$ which is Eq. (A2):

$$
\frac{\alpha A\omega}{\sqrt{2}\delta} \left[\coth(\alpha L) \sin\left(\frac{\pi}{4} - \alpha x + y\omega\right) - \coth(\alpha L) e^{-L/\delta} \cos\left(\frac{\pi}{4} - L/\delta - \alpha x + y\omega\right) \right.
$$

$$
\left. + \operatorname{csch}(\alpha L) \sin\left(\frac{\pi}{4} - \alpha x + y\omega\right) - \operatorname{csch}(\alpha L) e^{-L/\delta} \sin\left(\frac{\pi}{4} - L/\delta - \alpha x + y\omega\right) \right]. \quad (\text{A2})
$$

One can see that the resulting error is small for the parameter range of our model, as the error difference of the boundaries scales by $\sqrt{\nu/\omega L^2}$, which is inversely proportional to Reynolds number.

APPENDIX B: SYMMETRIC CASE

It is also possible to model the problem analytically for the case of symmetric deformations. This geometry has been studied often, as discussed in Sec. I. The symmetric model may offer more accuracy depending on the system of interest.

The only change from the asymmetric model is that the bottom boundary condition for the traveling sine wave case is defined as

$$
\psi_x^*(\chi, -L) = A\omega \sin(\alpha\chi).
$$

The solution then changes to be

$$
\psi^* = \frac{A\omega \operatorname{csch}(\mu L) \cos(\mu\chi) \sinh(\mu y)}{\mu}.
$$

The boundary layer correction can also be implemented by following the same procedure as for the asymmetric case in Sec. II.

Some notable differences between the asymmetric and symmetric case are the following: The amplitude is effectively doubled given how we have described the boundary condition, and reflux occurs near both moving boundaries.

A significant number of studies focus on the symmetric case, but the difference in the induced flow is not very significant. We present both cases so readers can apply the model that best fits their interest.

APPENDIX C: LAGRANGIAN FIELD EXPRESSION

To calculate the Lagrangian mean field we apply Eq. (18). One obtains the following expression:

$$
\begin{aligned}
U_{Lag} = \frac{1}{2}\pi A^2 \delta e^{-\frac{2(L+y)}{\delta}} \Bigg\langle & 2\alpha\delta e^{\frac{4y}{L}} \coth^2(\alpha L) \\
& - 4\alpha\delta \coth(\alpha L)\operatorname{csch}(\alpha L)e^{\frac{L+3y}{\delta}} \cosh(\alpha y) \cos\left(\frac{L-y}{\delta}\right) \\
& - 2\alpha\delta e^{\frac{2L}{\delta}} \operatorname{csch}^2(\alpha L)\left[2e^{\frac{y}{\delta}} \cosh(\alpha y) \cos\left(\frac{y}{\delta}\right) - 1\right] \\
& - \operatorname{csch}(\alpha L)e^{\frac{L+2y}{\delta}} \Bigg\{ 2\alpha\delta e^{\frac{L}{\delta}} \operatorname{csch}(\alpha L) \cosh(2\alpha y) \\
& \times (\alpha^2\delta^2 + 2) + e^{\frac{y}{\delta}} \coth(\alpha L) \sinh(\alpha y) \cos\left(\frac{L-y}{\delta}\right) \Bigg\} \\
& + \operatorname{csch}(\alpha L)e^{\frac{2L+y}{\delta}} \sinh(\alpha y)(\alpha^2\delta^2 + 2)\operatorname{csch}(\alpha L) \cos\left(\frac{y}{\delta}\right) \\
& + \coth(\alpha L) \sin\left(\frac{L-y}{\delta}\right)\Bigg\{ 2\alpha^2\delta^2 e^{\frac{4y}{\delta}} \coth(\alpha L) \sin\left(\frac{L-y}{\delta}\right) \\
& + (\alpha^2\delta^2 - 2)2e^{\frac{2+L}{\delta}} \operatorname{csch}(\alpha L) \sin\left(\frac{y}{\delta}\right) \Bigg\} \Bigg\rangle
\end{aligned}
$$

This expression gives a velocity field for particle drift in the x direction. The field is x independent.

---

[1] J. N. J. Lozano, *Peristaltic Flow with Application to Ureteral Biomechanics* (Citeseer, Princeton, NJ, 2009).

[2] J. Arrieta, J. H. E. Cartwright, E. Gouillart, N. Piro, O. Piro, and I. Tuval, Geometric mixing, peristalsis, and the geometric phase of the stomach, PLoS ONE **10**, e0130735 (2015).

[3] S. B. Hladky and M. A. Barrand, Mechanisms of fluid movement into, through and out of the brain: Evaluation of the evidence, Fluids Barriers CNS **11**, 26 (2014).

[4] H. Mestre, J. Tithof, T. Du, W. Song, W. Peng, A. M. Sweeney, G. Olveda, J. H. Thomas, M. Nedergaard, and D. H. Kelley, Flow of cerebrospinal fluid is driven by arterial pulsations and is reduced in hypertension, Nat. Commun. **9**, 1 (2018).

[5] B. F. Zagadou and D. C. Mountain, Analysis of the cochlear amplifier fluid pump hypothesis, J. Association Res. Otolaryngol. **13**, 185 (2012).

[6] E. Edom, D. Obrist, and L. Kleiser, Steady streaming in a two-dimensional box model of a passive cochlea, J. Fluid Mech. **753**, 254 (2014).

[7] M. Shokrian, C. Knox, D. H. Kelley *et al.*, Mechanically facilitated micro-fluid mixing in the organ of Corti, Sci. Rep. **10**, 14847 (2020).

[8] L. Sumner, J. Mestel, and T. Reichenbach, Steady streaming as a method for drug delivery to the inner ear, Sci. Rep. **11**, 1 (2021).

[9] A. H. Shapiro, M. Y. Jaffrin, and S. L. Weinberg, Peristaltic pumping with long wavelengths at low Reynolds number, J. Fluid Mech. **37**, 799 (1969).

[10] M. Y. Jaffrin and A. H. Shapiro, Peristaltic pumping, Annu. Rev. Fluid Mech. **3**, 13 (1971).

[11] Y. C. Fung and C. S. Yih, Peristaltic transport, J. Appl. Mech. **35**, 669 (1968).

[12] K. Ayukawa, T. Kawai, and M. Kimura, Streamlines and path lines in peristaltic flow at high Reynolds numbers, Bull. JSME **24**, 948 (1981).

[13] S. Takabatake, K. Ayukawa, and A. Mori, Peristaltic pumping in circular cylindrical tubes: A numerical study of fluid transport and its efficiency, J. Fluid Mech. **193**, 267 (1988).

[14] S. Takabatake and K. Ayukawa, Numerical study of two-dimensional peristaltic flows, J. Fluid Mech. **122**, 439 (1982).

[15] K. P. Selverov and H. A. Stone, Peristaltically driven channel flows with applications toward micromixing, Phys. Fluids **13**, 1837 (2001).

[16] X. Qing and M. Damodaran, Computational modelling of non-Newtonian effects on flow in channels with moving wall indentations, Int. J. Comput. Fluid Dyn. **15**, 329 (2001).

[17] Q. Xiao and M. Damodaran, A numerical investigation of peristaltic waves in circular tubes, Int. J. Comput. Fluid Dyn. **16**, 201 (2002).

[18] H. Yasmin, N. Iqbal, and A. Tanveer, Engineering applications of peristaltic fluid flow with Hall current, thermal deposition and convective conditions, Mathematics **8**, 1710 (2020).

[19] G. I. Taylor, Analysis of the swimming of microscopic organisms, Proc. R. Soc. London, Ser. A **209**, 447 (1951).

[20] D. G. Andrews and M. McIntyre, An exact theory of nonlinear waves on a Lagrangian-mean flow, J. Fluid Mech. **89**, 609 (1978).

[21] W. Thielicke and E. J. Stamhuis, Pivlab – Towards user-friendly, affordable and accurate digital particle image velocimetry in matlab, J. Open Res. Software **2**, e30 (2014).

[22] D. H. Kelley and N. T. Ouellette, Using particle tracking to measure flow instabilities in an undergraduate laboratory experiment, Am. J. Phys. **79**, 267 (2011).

[23] J. Chung and G. M. Hulbert, A time integration algorithm for structural dynamics with improved numerical dissipation: The generalized-α method, J. Appl. Mech. **60**, 371 (1993).

[24] J. Lighthill, Acoustic streaming in the ear itself, J. Fluid Mech. **239**, 551 (1992).

[25] D. Manoussaki and R. S. Chadwick, Effects of geometry on fluid loading in a coiled cochlea, SIAM J. Appl. Math. **61**, 369 (2000).

[26] D. Manoussaki, R. S. Chadwick, D. R. Ketten, J. Arruda, E. K. Dimitriadis, and J. T. O'Malley, The influence of cochlear shape on low-frequency hearing, Proc. Natl. Acad. Sci. **105**, 6162 (2008).

[27] J. Allen, Two-dimensional cochlear fluid model: New results, J. Acous. Soc. Am. **61**, 110 (1977).

[28] C. R. Steele and L. A. Taber, Comparison of WKB and finite difference calculations for a two-dimensional cochlear model, J. Acoust. Soc. Am. **65**, 1001 (1979).

[29] Y. Wang, C. R. Steele, and S. Puria, Cochlear outer-hair-cell power generation and viscous fluid loss, Sci. Rep. **6**, 1 (2016).

[30] A. Sasmal and K. Grosh, Unified cochlear model for low-and high-frequency mammalian hearing, Proc. Natl. Acad. Sci. **116**, 13983 (2019).

[31] K. Ohyama, A. N. Salt, and R. Thalmann, Volume flow rate of perilymph in the guinea-pig cochlea, Hearing Res. **35**, 119 (1988).

[32] S. M. Flaherty, I. J. Russell, and A. N. Lukashkin, Drug distribution along the cochlea is strongly enhanced by low-frequency round window micro vibrations, Drug Delivery **28**, 1312 (2021).

[33] K. D. Karavitaki and D. C. Mountain, Evidence for outer hair cell driven oscillatory fluid flow in the tunnel of Corti, Biophys. J. **92**, 3284 (2007).

[34] D. E. Troyetsky, J. Tithof, J. H. Thomas, and D. H. Kelley, Dispersion as a waste-clearance mechanism in flow through penetrating perivascular spaces in the brain, Sci. Rep. **11**, 4595 (2021).

[35] G. I. Taylor, Dispersion of soluble matter in solvent flowing slowly through a tube, Proc. R. Soc. London, Ser. A **219**, 186 (1953).

[36] I. Frankel and H. Brenner, On the foundations of generalized Taylor dispersion theory, J. Fluid Mech. **204**, 97 (1989).

Correction: Author surnames in Ref. [34] were displayed incorrectly and have been fixed.